Limitations in one-dimensional (an)elastic Earth models for explaining GPS-observed M_2 Ocean Tide Loading displacements in New Zealand

B. Matviichuk[1], M. A. King[1], C. S. Watson[1] and M. S. Bos[2*]

[1]School of Technology, Environments and Design, University of Tasmania,Hobart, 7001, Australia
[2]Instituto Dom Luiz (IDL), University of Beira Interior, Covilhã, Portugal

Key Points:

- M_2 ocean tide loading displacements in New Zealand are inferred from GPS observations
- Estimates for the North Island are not reproduced by models combining ocean tide loading and a 1D (an)elastic Earth structure.
- Spatially-coherent residual displacements of ∼0.4 mm (2%) are likely due to lateral Earth structure associated with Pacific Plate subduction

*supported by the project FCT/UIDB/50019/2020 – IDL funded by FCT

Corresponding author: B. Matviichuk, `bogdan.matviichuk@utas.edu.au`

Abstract

[GPS observations of ocean tide loading displacements can help infer the regional anelastic properties of the asthenosphere. We estimate M_2 ocean tide loading displacements at 170 GPS sites in New Zealand and compare these to modeled values using a range of numerical tide and radially symmetric (1D) elastic and anelastic Earth models. Regardless of the model combination we are unable to reduce the strong spatial coherence of the M_2 residuals across the North Island where they reach 0.4 mm (2%). The best fit in the North Island is obtained when combining the FES2014b tide model with spatially-variable ocean density and water compressibility, and the STW105 Earth model. The residuals exhibit a change of $\sim$0.3 mm in magnitude between the Taupo Volcanic Zone and the east coast ($\sim$100 km), suggesting that this region's laterally-varying, shallow rheological structure may need to be considered to explain these observations.]

Plain Language Summary

[The solid Earth changes shape due to the changing weight of the ocean as the ocean tides rise and fall. Measuring this change and comparing it to predictions can yield insights into the interior properties of the Earth, tens to hundreds of kilometers below the surface. We used GPS to measure the changing shape of New Zealand and compared it to predictions based on a range of Earth and tide models. The difference between the observed and modeled displacements revealed a complicated pattern over New Zealand, especially in the North Island and specifically near the Taupo Volcanic Zone. Due to the high accuracy of our GPS analysis and the complex geological structure of the region, we observed the limitations of modeling the loading of the solid Earth by a simple model that varies only with depth.]

1 Introduction

The asthenosphere, the weak viscoelastic substrate beneath the lithosphere, is fundamental to the concept of plate tectonics and the earthquake cycle (Hu et al., 2016). The rheological properties of the asthenosphere are, however, not well understood (Karato, 2012). The importance of the asthenosphere is amplified at active convergent boundaries of tectonic plates, specifically subduction systems that initiate forces principal in driving plate tectonics and mantle convection (Stern, 2004). New Zealand is split by the transform Alpine Fault and is locked between two subduction systems: Hikurangi in the north and Puysegur in the south (Lamarche & Lebrun, 2000). These lithospheric discontinuities should produce the largest perturbations observable on the earth tide and perhaps the ocean load tide (Zürn et al., 1976).

Analysis of Ocean Tide Loading (OTL) displacements, a phenomenon created by the solid Earth's response to tidal-water mass redistribution, can be measured by GPS and such measurements have been used to validate different ocean tide models and elastic Earth models at tidal periods (e.g., Martens et al., 2016; Yuan et al., 2013; Yuan & Chao, 2012). More recently these measurements have been used to constrain the asthenosphere's anelasticity at the period of the major M_2 tidal constituent (period of 12.42 h) by showing improved agreement with deformation modeled using anelastic Earth models. To date, studies of asthenosphere anelasticity have focused on continental settings such as western Europe, western USA, South America, the eastern China Sea region and Alaska (Bos et al., 2015; Ito & Simons, 2011; Martens & Simons, 2020; Wang et al., 2020).

In this paper, we examine the tidal deformation of New Zealand, at the dominant M_2 tidal period, using an array of continuous GPS stations. We combine recent ocean tide models with a range of purely elastic and anelastic Earth models and compare modeled deformation with GPS observed estimates to further understand the anelastic properties of the asthenosphere beneath New Zealand.

2 Methods

2.1 GPS Data and Analysis

We analyzed all available continuously operating GNSS stations in New Zealand over the period 2013 001 to 2020 153, chosen to maximize the common period of GPS observations. Over this seven-year period, data are available from 170 stations, with all but two (CHTI and RAUL) on mainland New Zealand (see Table S1 for a full list of sites). These stations were designed for nationwide coverage with station spacing in the range 80–100 km to monitor and control the national datum and for geophysical studies (Gale et al., 2015). As shown in Fig. 1, the network provides approximately uniform (but sparse) coverage in the South Island with a substantially higher spatial density of coverage across much of the North Island.

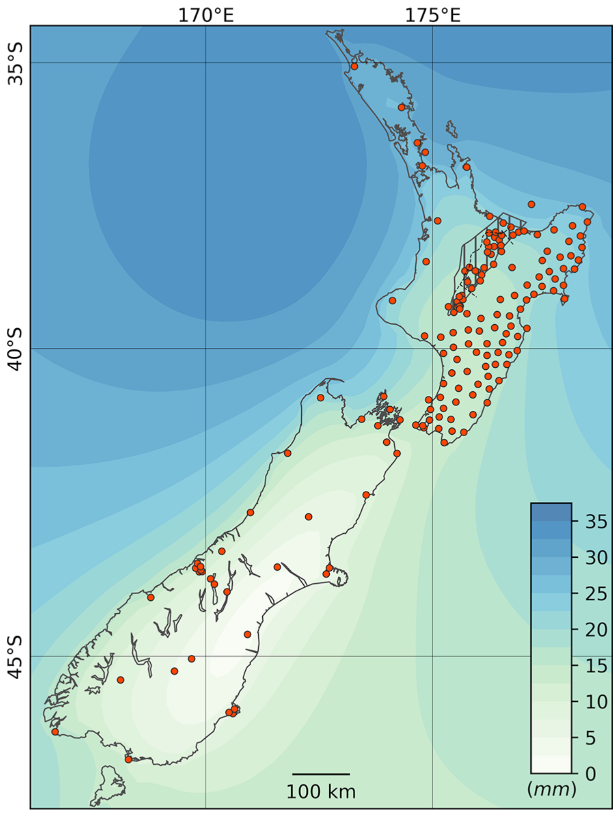

Figure 1. Map of New Zealand showing modeled M_2 Up OTL displacement computed with TPXO7.2 ocean tide model and PREM Green's function. GNSS sites are represented by orange circles. The hatched area in the North Island represents the approximate region of the Taupo Volcanic Zone.

These data were analyzed using GipsyX v1.3 software (Bertiger et al., 2020) using a quite standard kinematic Precise Point Positioning (PPP) approach (Zumberge et al., 1997). The dataset processing was fascilitated by a custom wrapper (Matviichuk, 2020). Our approach was described in full by Matviichuk et al. (2020) with the main difference being that we used only the GPS data. Data from other GNSS (e.g. GLONASS) were not logged at all sites over this period hence was excluded from this analysis. We used NASA JPL's orbit and clock products from their third internal reprocessing campaign (repro 3.0, released March 2018). Ambiguities were fixed to integers where possible (Bertiger et al., 2010). Earth body tides were modeled within GipsyX according to IERS 2010 Conventions (Petit & Luzum, 2010).A priori OTL values were removed based on the FES2004 ocean tide model (Lyard et al., 2006) and Gutenberg-Bullen purely-elastic Earth model (Farrell, 1972) in a centre-of-mass of the whole Earth system frame (http://holt.oso.chalmers.se/loading) – we later restored the OTL component at the coordinate time series level for further study; this remove-restore approach is done to reduce the magnitude of companion tides and follows approaches adopted previously (e.g., Abbaszadeh et al., 2020; Matviichuk et al., 2020; Penna et al., 2015).

The GipsyX coordinate and zenith-wet-delay process noise values were chosen based on the tests of Penna et al. (2015), Wang et al. (2020) and Matviichuk et al. (2020), using values of 3.2 mm/sqrt(s) and 0.1 mm/sqrt(s), respectively. Our parameterization produces coordinate estimates every 300 s from which we remove large outliers identified with clock bias estimates larger than $3{\times}10^3$ meters and residuals to a linear trend larger than $\pm3\sigma$ of each global cartesian coordinate component. These timeseries were converted to local topocentric east, north and up components which were then further analyzed.

2.2 OTL Models

We focus here on the difference between the GPS-derived OTL displacements and those modeled based on ocean tide models and elastic and anelastic Earth models. For the tides we mainly consider three relatively recent global ocean tide models: GOT4.10c (Ray, 2013), TPXO9.v1 (Egbert & Erofeeva, 2002) and FES2014b (Carrere et al., 2016), although we also explore FES2012 (Carrere et al., 2013) and FES2004 (Lyard et al., 2006). We also consider one regional New Zealand tide model (Walters et al., 2001), EEZ, which we combine with FES2014b outside the model's domain for loading computations.

The M_2 tide reaches over 1 m near the coast of New Zealand, due to the shallow bathymetry, and decreases to 10-20 cm in the open ocean (Stammer et al., 2014). The pattern of M_2 between the two islands of New Zealand acts like an amphidromic point although the amplitudes are not zero. As a result, the tides to the east and west of New Zealand are out of phase and partly cancel out each other's contribution to the total OTL value.

All modeled OTL values were computed using the CARGA software (Bos & Baker, 2005). The coastline was taken from the GMT database (Wessel & Smith, 1996) and has a resolution of around 150 m. In most studies a constant sea water density is assumed, for example 1030 kg/m$_3$. Ray (2013) advocated to take the spatial variation of the density into account, and even the fact that water is slightly compressible, which means that the mean density of a water column should increase due to the extra density at the bottom of the column. For the ocean around New Zealand the effect on the resultant deformation is around 1-3%. Assuming a mean 2% effect and a mean OTL amplitude of 20 mm, this corresponds to a potential error of 0.4 mm which is too large to be ignored. We have implemented the equations of Ray (2013) and obtained mean density values from the World Ocean Atlas 2013 - WOA13 (Zweng et al., 2013)based on a $0.25{\times}0.25°$ grid.

Three Green's functions were assessed with this set of ocean tide models: PREM (Dziewonski & Anderson, 1981), STW105 (Kustowski et al., 2008) and S362ANI (Kustowski et al., 2008). PREM and STW105 provide radial (1D) profiles for the density, and seismic velocities Vp and Vs. These profiles were used to compute load Love numbers which were converted into Green's functions (Bos & Scherneck, 2013). The method is based on Alterman et al. (1959) but uses the more recent Chebyshev collocation method to solve the differential equations (Guo et al., 2001). These profiles are based on seismic data and are only valid at a period of 1 s. To convert them to the period of harmonic M_2, a constant absorption band (Q=constant, see Table S5) is assumed between these two periods (Bos et al., 2015). S362ANI is based on STW105 but has a shear velocity that varies horizontally, not just by depth. We averaged the values in a rectangular region between 48°S and 33°S and 165°E and 180°E to yield a model representative of the average values over the study region. Once converted into a radially symmetric model, the Green's function for S362ANI was computed in similar manner as PREM and STW105.

2.3 OTL Analysis

Amplitudes and phases of tidal constituents were estimated from the timeseries using the Eterna software v.3.30 (Wenzel, 1996) for 17 tidal constituents, with local phases converted to Greenwich phases with lags positive to compare with the models of OTL displacement. Our focus is solely on the largest loading constituent in New Zealand, M_2, the major semi-diurnal lunar constituent. To decrease the computation time and measurement noise, the timeseries were first downsampled to 30-min through window averaging.

We follow the naming conventions of Yuan and Chao (2012) with observed and modeled OTL referred to as Z_{obs} and Z_{OTL} respectively with Z_{res} being their vector difference. We refer to the magnitude of the vector difference as $\|Z_{res}\|$.

3 Results

3.1 Preliminary analysis of the ocean tide models

To better understand the variation between recent global ocean tide models at the M_2 period we compute the mean ocean tide model (Fig. S1a) and inter-model standard deviation (Fig. S1b) using the three more recent ocean tide models: FES2014b, GOT4.10c, and TPXO9.v1. We found M_2 SD values of 0.18 cm and 2.68 cm for the deep ocean (>1000 m depth) and the shallow sea (¡ 1000 m depth) respectively. These values are smaller by 40% and 20% than globally derived values reported byStammer et al. (2014) for M_2. The largest SD values of up to 0.6 m are located in the Hauraki Gulf in the western North Island, which indicates the region where the largest ocean tides errors are expected.

We compared FES2004 and EEZ models with a mean ocean tide model, specified above (Fig. S2) by computing a vector difference grids. FES2004 has higher discrepancies (up to 1 m) in the semi-closed water bodies and shallow bights (e.g. South and North Taranaki bights, Fig. S2a), while the EEZ regional tide model shows an approximately constant vector difference in the shallow sea waters (¡ 1000 m) of around 0.1 m (Fig. S2b).

3.2 Comparison of GPS and PREM-based Models

The GPS-estimated M_2 OTL displacements (with the a priori model restored) are shown in Fig. S3 and listed in Table S2 for each of the up, north and east components. These show a spatially coherent signal across New Zealand with the amplitude ranging from 2 (WAIM) to 32 (KTIA) mm. Using these observations and the modeled Z_{OTL} based on FES2014b and PREM we computed Z_{res} as shown in Fig. 2a. M_2 up residuals in the North Island are significant and demonstrate a spatially coherent amplitude of ∼1 mm and phase residual of ∼-10° while residuals in the South Island are small but harder to interpret due to the lower station density and the low OTL amplitude (Fig. 1). This is consistent across different global ocean tide models as indicated by the $\|Z_{res}\|$ values summarized in the boxplots (Fig. 2c, S4-5). $\|Z_{res}\|$ variation over the range of tide models with PREM has median value of around 0.7 mm for any of the global tide models while the median for EEZ is ∼2 mm. This bias within the EEZ model results in a spatially coherent signal evident from the phasor maps (Fig. S6.2, up component), especially in the North Island.

While all the recent global ocean tide models perform similarly in the horizontal components, FES2014b demonstrates the largest reduction of $\|Z_{res}\|$ over the set of Green's functions in the up component (Fig. S5). Thus, we continue with FES2014b (Fig. 2c) as a baseline ocean tide model for the subsequent tests.

We considered the impact on the total OTL of specific water bodies by dividing the global oceans into nine separate water areas surrounding New Zealand (Fig. S1). To illustrate the influence of different regions, we selected three sites that experience high, moderate and low M_2 OTL: KTIA, RGMT and MQZG, respectively (Fig. 3). The set of ocean tide models considered consists of the three recent global atlases (FES2014b,

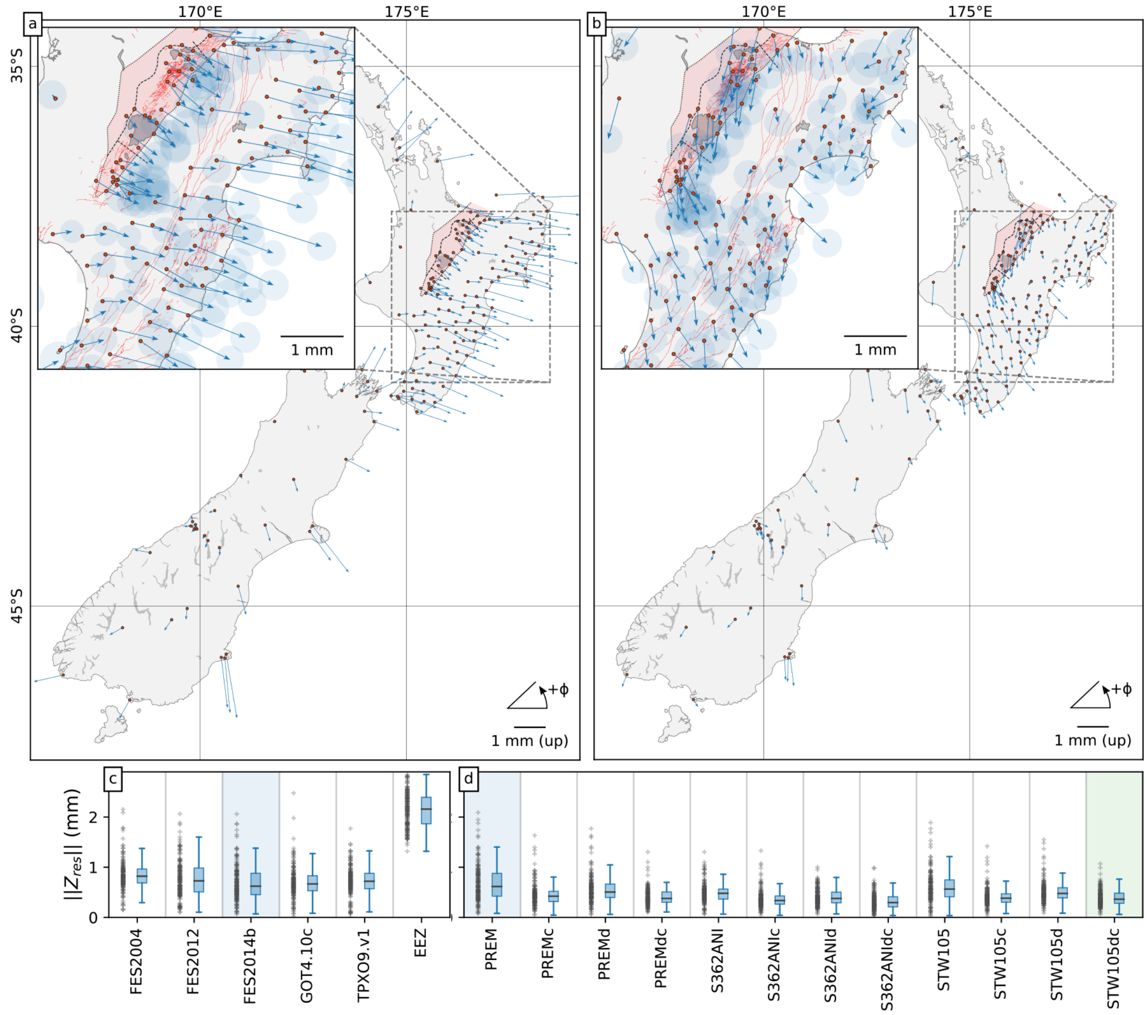

Figure 2. M_2 OTL residuals relative to FES2014b_PREM (a), FES2014_STW105dc (b) and residual magnitude ($\|Z_{res}\|$) boxplots for different model setups (c, d). The horizontal line on each box is the median value, the box represents the inter-quartile range (IQR) and the whiskers show an additional 1.5×IQR. Blue and green shading highlights boxplots of (a) and (b) maps, respectively. The Earth model suffixes 'd' and 'c' in panel (d) refer to the additional treatment of dissipation and compressibility, respectively.

TPXO9.v1 and GOT4.10c), FES2012 and EEZ. The latter produces ∼2 mm residual amplitude (purple symbols in Fig. 3) and is thus excluded from further analysis. The other models show closer agreement but in general outside the observation 95% confidence interval when using PREM (Fig. 3, bottom panels). However, we note the similar magnitude of the variance in $\|Z_{res}\|$ for all models including EEZ (when the bias is ignored) in the up component and complete absence of a $\|Z_{res}\|$ bias in the horizontal components (Fig. S5).

Residuals using the purely elastic STW105 show a similar level of variance and median as PREM (Fig. 2d) while S362ANI has 50% reduced variance and slightly reduced median (0.48 mm compared with 0.61 mm for PREM). However, neither model produces consistent agreement within the GPS uncertainty as shown, for example with the three sites presented in Fig. 3. We next explore the sensitivity of the modeled OTL to anelastic dissipation (denoted suffix "d"), and spatially-varying ocean density and compressibility ("c").

3.3 Effect of Considering Anelasticity (Dissipation)

Bos et al. (2015) demonstrated that accounting for some of the effects of M_2 mantle anelasticity by modifying the Green's functions to include dissipation, decreased OTL residuals in western Europe by up to 0.2 mm. Matviichuk et al. (2020) confirmed these results for the same region but using a different time frame, while similar results have been found by Wang et al. (2020) for south-east Asia.

For New Zealand, we find a reduction of $\|Z_{res}\|$ variance and median for all Earth models when dissipation is included (Fig. 2d). The effect is illustrated in Fig. 3 where the models including dissipation (squares with left side only filled) are shown to be closer to the GPS estimates. These do, however, remain outside the GPS 95% confidence interval. At the same time as this improvement, we noticed the introduction of up to 0.2 mm $\|Z_{res}\|$ bias into the north component with dissipation enabled, independent of the Green's function used; the east component also shows this effect but only with S362ANI (Fig. S4). Enabling sea water compressibility correction partially suppresses the bias. We discuss this further below.

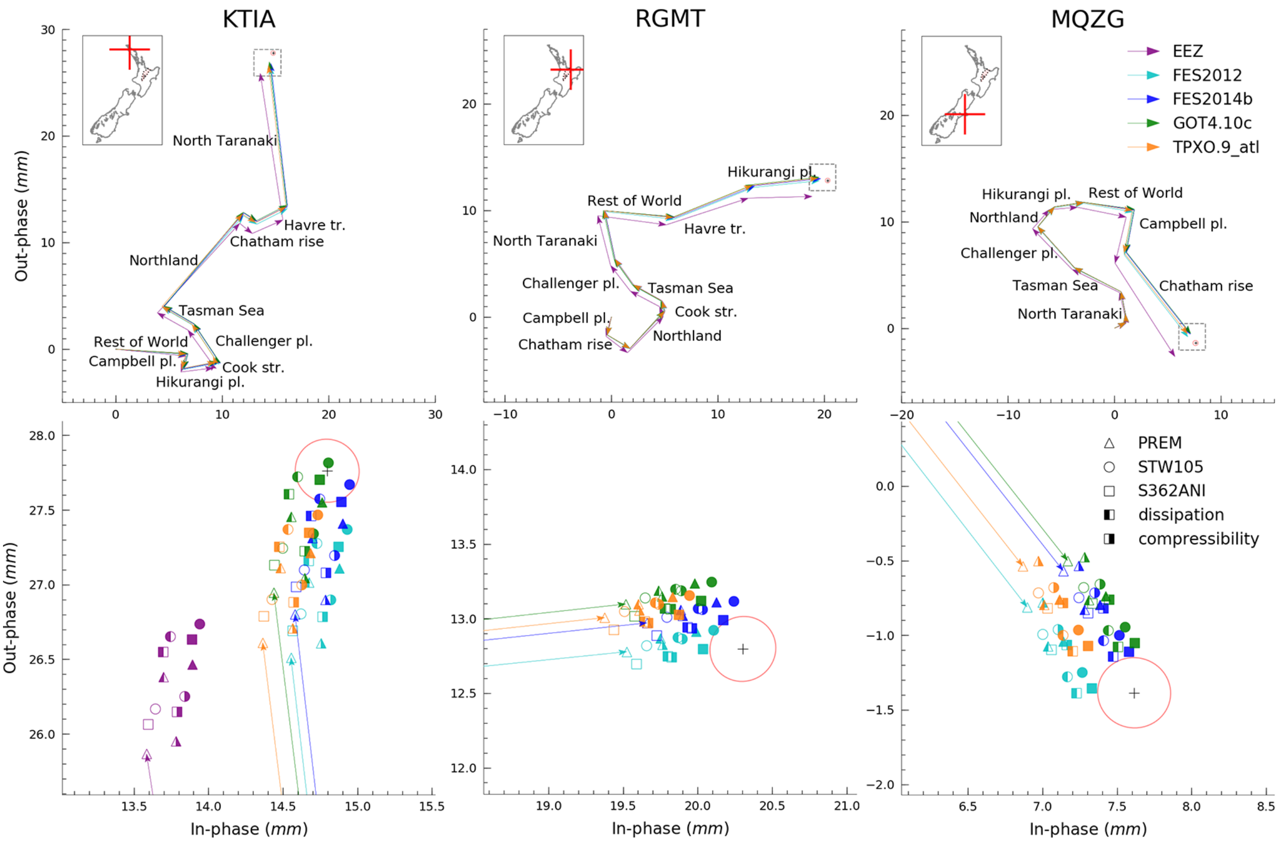

Figure 3. Phasor plots of the OTL contributions from different oceanic regions (see Fig. S1) for M_2 Up displacements computed with various Green's functions and ocean tide models. The right bottom panels show the detail for the vector tip as highlighted in the respective left top panels. GPS observations are shown with a black "+" and 95% confidence interval as a red circle. OTL produced by the outside area is titled as "rest of the world".

3.4 Assessment of Water Density and Compressibility Correction

Enabling the seawater compressibility correction decreases the median $\|Z_{res}\|$ by a further ∼0.2 mm in the up component, as shown in Fig. 2d and by example in Fig. 3 (fully filled symbols). In some cases, the application of both dissipation and compressibility eliminates the residual in the up component, although as we discuss in the next section, large, regionally coherent residuals persist. Horizontal components show an increase in variance (Fig. S4) with only compressibility. The dissipation-introduced $\|Z_{res}\|$ bias in the north component can be partially (S362ANIdc) or completely (PREMdc, STW105dc) removed by additionally applying the compressibilty correction (Fig. S4-5, FES2014b). The east component shows a marginal (less than 0.1 mm) increase in both $\|Z_{res}\|$ median and variance over the solutions with just dissipation included for PREM and STW105, while S362ANI shows further dissipation-introduced increase in $\|Z_{res}\|$ bias by another 0.1 mm (Fig. S4).

Following Martens and Simons (2020), we constructed Empirical Cumulative Distribution Function (ECDF) plots (Fig. S7.1). The ECDF analysis shows the expected behavior of the corrections in the up component: each correction increases the slope of the ECDF indicating successive improvement with each correction. This is not the case for the horizontal components where both corrections introduce biases using S362ANI, which otherwise demonstrates performance comparable to other models without the corrections. The optimum correction of PREM and STW105 in the north component very much relies on the selection of ocean tide model. The dissipation-introduced bias is suppressed by the compressibility correction in the case of FES2014b and GOT4.10c, which suggests the best performance with both dissipation and compressibility corrections enabled. In the case of TPXO9.v1, the bias is too large for compressibility to overcome, effectively repeating the trend as observed for S362ANI.

Removing the respective mean Z_{res} values from each set of residuals (Fig. S7.2) aligns the ECDFs over all components, fully removing the differences in the horizontal components with exception for S362ANI-based values in the north component. Removing mean Z_{res} also absorbs any long-wavelength errors in the solid Earth body tide.

4 Discussion

Following these tests, the optimal agreement between the observed and modeled OTL in all three components occurs when using FES2014b and STW105dc. The spatial distribution of Z_{res} shows ∼0.5 mm residual spatially coherent field over the Taupo Volcanic Zone (TVZ) Z_{res} in the North Island, as shown in Fig. 4. The dense coverage of stations in these regions reveals a distinct change of Z_{res} between sites in the East Coast (EC) and TVZ that experience the same M_2 OTL (Fig. 1).

To aid discussion, we consider four different regions (blocks) within this region as illustrated by the symbols in Fig. 4: TVZc, TVZs, ECc, ECs, with "c" and "s" subscripts identifying central and southern subareas, respectively. Residual OTL in each block was averaged to provide Z_{res} summary metrics (per component) relevant to each region (Table S6). Note that several sites along the EC were removed (e.g. Hawke Bay) as they experience a localized signal (Fig. 4, black symbols) which is independent of the ocean tide model or Green's function used. The sites in both TVZ regions show residual amplitudes of ∼0.5 mm with phase changing sharply from -102° to -70° between TVZc and TVZs. The relative phase change between TVZ and EC within the same central or south area (TVZc/ECc and TVZs/ECs) is found to be approximately constant (∼35°) while revealing 0.25 mm and 0.15 mm larger amplitudes for TVZc and TVZs, respectively.

The sharp change in residual phase between TVZc and TVZs , and the strong spatial variation in residual amplitude between respective EC and TVZ sub-regions over length-scales of the order of ∼100 km suggests that the variations are due to localized effects. We discount errors in ocean tides given our previous tests and the spatial distribution

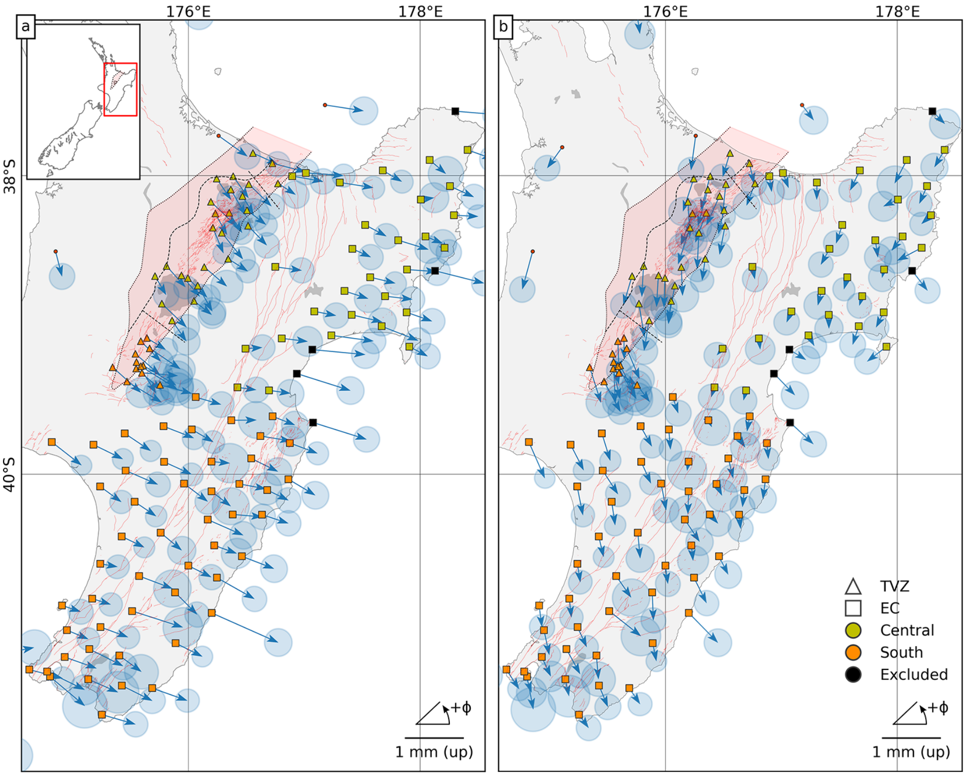

Figure 4. GPS-derived M_2 OTL residuals for a section of the North Island relative to FES2014b ocean tide model combined with dissipation corrected STW105d (a) and STW105dc (b). "d" and "c" suffixes stand for dissipation and compressibility corrections. Sites are categorized into Taupo Volcanic Zone (TVZ) and East Coast (EC) regions (symbol shape) with subdivision of each into central and south along the TVZ central/south boundary (symbol color).

of the residuals. Also, biases in the adopted deep Earth rheological structure (Lau et al., 2017) would be effectively constant over this area.

Instead, our assumption is that the residuals result from mismodeled shallow-Earth rheological structure. To explore this further, we iterate through a range of alternative Earth models with different rheological structure in the upper tens of kilometers based on seismic tomography inversions (Eberhart-Phillips & Bannister, 2015; Eberhart-Phillips & Fry, 2018). No single one-dimensional (radially-varying) Earth model could explain the regional pattern of residuals, with changes generally producing changes that were spatially uniform across the region of Fig. 4.

Deviations in the shallow rheological structure from that used to compute the Earth body tides could produce localized residuals. (Zürn et al., 1976) developed a 2D finite-element model of a subduction zone in Alaska, and showed that the subduction zone structure can produce an effect up to 0.8% on the solid Earth body tide in the radial direction directly above the asthenospheric slab. For M_2 at the latitude of the North Island, this equates to 0.7 mm. However, their modeling also showed that the maximum gradient over the distance from East coast to TVZ (up to 150 km) should not exceed 0.25%. We note that the effect on phase is not described in their work. However, if we consider the relative location of the TVZ over the subduction slab (observed by the Vp anomaly at 100-130 km depth (Eberhart-Phillips & Fry, 2018)), the maximum expected change becomes close to 0.15%, or 0.13 mm for M_2 at these latitudes. As such, this is well below the magnitude of the variations seen in Fig. 4.

The effect of lateral rheological structure on modeled OTL is unclear. However, modeling of elastic deformation due to longer-period surface mass displacement indicates that consideration of global, localized Earth structure produced differences of the order 10% in the vertical and 20% in the horizontal over distances of 10-50 km (Dill et al., 2015). The average M_2 OTL in the region of the TVZ shown in Fig. 4 is ∼19 mm and so even a 2% effect due to lateral variation may be relevant to explaining the observed residuals. Given the minor, but non-negligible effect of lateral variation on Earth body tides, and likely effects on OTL displacements, our analysis suggests that one-dimensional models of this region are unlikely to fully explain GPS observations of OTL at M_2. To check for potential long-wavelength errors that could introduce the observed dissipation-introduced biases in the horizontal components, we repeated our analyses for a set of 15 stations in the inland Australia (see Table S3 for site list and Table S4 for derived observations) where the geological setting is simpler and where a 1D model should produce accurate results. For this dataset we needed to adopt a different time period (2015-2018 inclusive) due to data availability but checking a subset of sites in New Zealand found time-period was inconsequential. Figures S9 and S10 demonstrate that, although the magnitude of the OTL is still several mm, for these stations the residuals (observed minus predicted OTL) are indeed small and within the uncertainty of the observations. This validates the correctness of our analyses and suggests that tidal centre-of-mass errors in this region are small.

Figures S7.1 and S7.2 show that the OTL residuals for the horizontal components suffer from some common mode problem but that modification of the Green's function cannot reduce the misfit. For the up component, the influence of the dissipation effect within asthenosphere that requires us to modify the elastic properties of the Earth model from the reference period of 1s to tidal periods is noticeable. Furthermore, including spatially varying seawater density and compressibility results in an additional reduction of the misfit. The two figures also demonstrate that the difference between the ocean tide models used in the loading computations is small. Therefore, the most likely candidate to reduce the misfit further reduction is using an advanced (3D) (an)elastic model of the region.

Similar problems using a 1D Earth modeling OTL loading in Alaska were recently described by Martens and Simons (2020). We are unaware of three-dimensional models being in use for the computation of OTL, however Latychev et al. (2009) have computed Earth Body tides with a three-dimensional model. One practical consequence of this is that mismodeled tidal deformations in this region will propagate into conventional 24 hr coordinate solutions (Penna et al., 2007). Such propagation will introduce long-period noise in GPS coordinate time series in New Zealand and impact subsequent geophysical interpretation.

5 Conclusions

We estimate M_2 ocean tide loading (OTL) displacements at 170 GPS sites in New Zealand between 2013 001 and 2020 153. Comparison with modeled OTL displacements using a range of global tide models and elastic PREM shows sub-mm agreement, with much larger disagreements using a local New Zealand tide model.

However, we find that the no single one-dimensional elastic Earth model, when combined with modern global tide models, can consistently explain the GPS-derived OTL within uncertainties. Of the tested ocean tide models, FES2014b produced the best results. However, application of an anelastic dissipation correction, and varying water density and compressibility substantially improves the agreement between the various models and observed OTL. Despite this, some regional spatially-coherent unmodeled residual signals remain in the North Island with magnitudes of up to 0.3 mm. These show substantial variation in phase over ∼100 km in the region between the Taupo Volcanic Zone and the East coast. We attempted to reproduce the observed signal using a range of 1D Earth models with varying shallow Earth structures, including the effects of anelasticity, however no single model could explain the residuals. We anticipate that these residuals are a result of unmodeled lateral variations in Earth rheological structure forced largely by ocean tide loading but with a smaller component likely from mismodeled Earth body tides.

This analysis of residual OTL demonstrates the deficiencies of the 1D Earth modeling approach that is currently standard practice. This is particularly relevant to GPS analysis using 24 hr coordinate solutions, given mismodeled tidal displacements propagate into long-period signal. Utilizing 3D Earth modeling to compute tidal phenomena is likely required to explain the observations in regions with major discontinuities in Earth's lateral structure (e.g. subduction margins). Such models, combined with these observations, could provide new insights into the shallow rheological structure of these regions.

Acknowledgments

We greatly acknowledge the New Zealand GeoNet project and its sponsors EQC, GNS Science and LINZ, and Geoscience Australia for providing the data used in this study. We are grateful to NASA Jet Propulsion Laboratory for GipsyX software, products and support. The services of TPAC High Performance Computing Facility are acknowledged gratefully. We thank Klaus Schueller for advice and discussion on Eterna software. We acknowledge the support of Elisabetta D'Anastasio in getting the data and sites' logs.

Bogdan Matviichuk is supported by Tasmania Graduate Research Scholarship. MSB is supported by the project FCT/UIDB/50019/2020 – IDL funded by FCT.

GipsyX binaries were provided under license from JPL. Eterna tidal analysis and prediction software with source code was acquired from International Geodynamics and Earth Tide Service (IGETS), igets.u-strasbg.fr/soft_and_tool.php.

References

Abbaszadeh, M., Clarke, P. J., & Penna, N. T. (2020). Benefits of combining GPS and GLONASS for measuring ocean tide loading displacement. *Journal of Geodesy*, *94*(7), 63. doi: 10.1007/s00190-020-01393-5

Alterman, Z., Jarosch, H., Pekeris, C. L., & Jeffreys, H. (1959). Oscillations of the earth. *Proceedings of the Royal Society of London. Series A. Mathematical and Physical Sciences*, *252*(1268), 80–95. doi: 10.1098/rspa.1959.0138

Bertiger, W., Bar-Sever, Y., Dorsey, A., Haines, B., Harvey, N., Hemberger, D., ... Willis, P. (2020). GipsyX/RTGx, a new tool set for space geodetic operations and research. *Advances in Space Research*, *66*(3), 469–489. doi: 10.1016/j.asr.2020.04.015

Bertiger, W., Desai, S. D., Haines, B., Harvey, N., Moore, A. W., Owen, S., & Weiss, J. P. (2010). Single receiver phase ambiguity resolution with GPS data. *Journal of Geodesy*, *84*(5), 327–337. doi: 10.1007/s00190-010-0371-9

Bos, M. S., & Baker, T. F. (2005). An estimate of the errors in gravity ocean tide loading computations. *Journal of Geodesy*, *79*(1), 50–63. doi: 10.1007/s00190-005-0442-5

Bos, M. S., Penna, N. T., Baker, T. F., & Clarke, P. J. (2015). Ocean tide loading displacements in western europe: 2. gps-observed anelastic dispersion in the asthenosphere. *Journal of Geophysical Research: Solid Earth*, *120*(9), 6540–6557. doi: 10.1002/2015JB011884

Bos, M. S., & Scherneck, H.-G. (2013). Computation of Green's Functions for Ocean Tide Loading. In G. Xu (Ed.), *Sciences of Geodesy - II* (pp. 1–52). Berlin, Heidelberg: Springer Berlin Heidelberg. doi: 10.1007/978-3-642-28000-9_1

Carrere, L., Lyard, F., Cancet, M., Guillot, A., & Dupuy, S. (2016). Fes 2014 : a new global tidal model. , 8.

Carrere, L., Lyard, F., Cancet, M., Guillot, A., & Roblou, L. (2013). Fes 2012: A new global tidal model taking advantage of nearly 20 years of altimetry. In *20 years of progress in radar altimetry* (Vol. 710, p. 13).

Dill, R., Klemann, V., Martinec, Z., & Tesauro, M. (2015). Applying local green's functions to study the influence of the crustal structure on hydrological loading displacements. *Journal of Geodynamics*, *88*, 14–22. doi: 10.1016/j.jog.2015.04.005

Dziewonski, A. M., & Anderson, D. L. (1981). Preliminary reference earth model. *Physics of the Earth and Planetary Interiors*, *25*(4), 297–356. doi: 10.1016/0031-9201(81)90046-7

Eberhart-Phillips, D., & Bannister, S. (2015). 3-d imaging of the northern hikurangi subduction zone, new zealand: variations in subducted sediment, slab fluids and slow slip. *Geophysical Journal International*, *201*(2), 838–855. doi: 10.1093/gji/ggv057

Eberhart-Phillips, D., & Fry, B. (2018). Joint local earthquake and teleseismic inversion for 3-d velocity and q in new zealand. *Physics of the Earth and Planetary Interiors*, *283*, 48–66. doi: 10.1016/j.pepi.2018.08.005

Egbert, G. D., & Erofeeva, S. Y. (2002). Efficient Inverse Modeling of Barotropic Ocean Tides. *Journal of Atmospheric and Oceanic Technology*, *19*(2), 183–204. doi: 10.1175/1520-0426(2002)019⟨0183:EIMOBO⟩2.0.CO;2

Farrell, W. E. (1972). Deformation of the earth by surface loads. *Reviews of Geophysics*, *10*(3), 761–797. doi: 10.1029/RG010i003p00761

Gale, N., Gledhill, K., Chadwick, M., & Wallace, L. (2015). The Hikurangi Margin Continuous GNSS and Seismograph Network of New Zealand. *Seismological Research Letters*, *86*(1), 101–108. doi: 10.1785/0220130181

Guo, J.-Y., Ning, J.-S., & Zhang, F.-P. (2001). Chebyshev-collocation method applied to solve odes in geophysics singular at the earth center. *Geophysical Research Letters*, *28*(15), 3027–3030. doi: 10.1029/2001GL012886

Hu, Y., Bürgmann, R., Banerjee, P., Feng, L., Hill, E. M., Ito, T., ... Wang, K. (2016). Asthenosphere rheology inferred from observations of the 2012 indian ocean earthquake. *Nature*, *538*(7625), 368–372. doi: 10.1038/nature19787

Ito, T., & Simons, M. (2011). Probing asthenospheric density, temperature, and elastic moduli below the western united states. *Science*, *332*(6032), 947–951. doi: 10.1126/science.1202584

Karato, S.-i. (2012). On the origin of the asthenosphere. *Earth and Planetary Science Letters*, *321-322*, 95–103. doi: 10.1016/j.epsl.2012.01.001

Kustowski, B., Ekström, G., & Dziewoński, A. M. (2008). Anisotropic shear-wave velocity structure of the earth's mantle: A global model. *Journal of Geophysical Research: Solid Earth*, *113*(B6). doi: 10.1029/2007JB005169

Lamarche, G., & Lebrun, J.-F. (2000). Transition from strike-slip faulting to oblique subduction: active tectonics at the puysegur margin, south new zealand. *Tectonophysics*, *316*(1), 67–89. doi: 10.1016/S0040-1951(99)00232-2

Latychev, K., Mitrovica, J. X., Ishii, M., Chan, N.-H., & Davis, J. L. (2009). Body tides on a 3-D elastic earth: Toward a tidal tomography. *Earth and Planetary Science Letters*, *277*(1), 86–90. doi: 10.1016/j.epsl.2008.10.008

Lau, H. C. P., Mitrovica, J. X., Davis, J. L., Tromp, J., Yang, H.-Y., & Al-Attar, D. (2017). Tidal tomography constrains Earth's deep-mantle buoyancy. *Nature*, *551*(7680), 321–326. doi: 10.1038/nature24452

Lyard, F., Lefevre, F., Letellier, T., & Francis, O. (2006). Modelling the global ocean tides: modern insights from FES2004. *Ocean Dynamics*, *56*(5-6), 394–415. doi: 10.1007/s10236-006-0086-x

Martens, H. R., & Simons, M. (2020). A comparison of predicted and observed ocean tidal loading in alaska. *Geophysical Journal International*, ggaa323. doi: 10.1093/gji/ggaa323

Martens, H. R., Simons, M., Owen, S., & Rivera, L. (2016). Observations of ocean tidal load response in south america from subdaily gps positions. *Geophysical*

Journal International, *205*(3), 1637–1664. doi: 10.1093/gji/ggw087

Matviichuk, B. (2020). *GipsyX Wrapper: v0.1.0.* doi: 10.5281/zenodo.4001166

Matviichuk, B., King, M. A., & Watson, C. (2020). Estimating ocean tide loading displacements with gps and glonass. *Solid Earth Discussions*, 1–23. doi: https://doi.org/10.5194/se-2020-22

Penna, N. T., Clarke, P. J., Bos, M. S., & Baker, T. F. (2015). Ocean tide loading displacements in western europe: 1. validation of kinematic gps estimates. *Journal of Geophysical Research: Solid Earth*, *120*(9), 6523–6539. doi: 10.1002/2015JB011882

Penna, N. T., King, M. A., & Stewart, M. P. (2007). Gps height time series: Short-period origins of spurious long-period signals. *Journal of Geophysical Research: Solid Earth*, *112*(B2). doi: 10.1029/2005JB004047

Petit, G., & Luzum, B. (2010). IERS Technical Note. (36), 179.

Ray, R. D. (2013). Precise comparisons of bottom-pressure and altimetric ocean tides: Bottom-pressure and altimetric tides. *Journal of Geophysical Research: Oceans*, *118*(9), 4570–4584. doi: 10.1002/jgrc.20336

Stammer, D., Ray, R. D., Andersen, O. B., Arbic, B. K., Bosch, W., Carrère, L., … Yi, Y. (2014). Accuracy assessment of global barotropic ocean tide models. *Reviews of Geophysics*, *52*(3), 243–282. doi: 10.1002/2014RG000450

Stern, R. (2004). Subduction initiation: spontaneous and induced. *Earth and Planetary Science Letters*, *226*(3-4), 275–292. doi: 10.1016/S0012-821X(04)00498-4

Walters, R. A., Goring, D. G., & Bell, R. G. (2001). Ocean tides around New Zealand. *New Zealand Journal of Marine and Freshwater Research*, *35*(3), 567–579. doi: 10.1080/00288330.2001.9517023

Wang, J., Penna, N. T., Clarke, P. J., & Bos, M. S. (2020). Asthenospheric anelasticity effects on ocean tide loading around the east china sea observed with gps. *Solid Earth*, *11*(1), 185–197. doi: 10.5194/se-11-185-2020

Wenzel, H.-G. (1996). The nanogal software : Earth tide data processing package eterna 3.30. *Bull. Inf. Marées Terrestres*, *124*, 9425–9439.

Wessel, P., & Smith, W. H. F. (1996). A global, self-consistent, hierarchical, high-resolution shoreline database. *Journal of Geophysical Research: Solid Earth*, *101*(B4), 8741–8743. doi: 10.1029/96JB00104

Yuan, L., & Chao, B. F. (2012). Analysis of tidal signals in surface displacement measured by a dense continuous gps array. *Earth and Planetary Science Letters*, *355-356*, 255–261. doi: 10.1016/j.epsl.2012.08.035

Yuan, L., Chao, B. F., Ding, X., & Zhong, P. (2013). The tidal displacement field at earth's surface determined using global gps observations: Tidal displacements determined by gps. *Journal of Geophysical Research: Solid Earth*, *118*(5), 2618–2632. doi: 10.1002/jgrb.50159

Zumberge, J. F., Heflin, M. B., Jefferson, D. C., Watkins, M. M., & Webb, F. H. (1997). Precise point positioning for the efficient and robust analysis of gps data from large networks. *Journal of Geophysical Research: Solid Earth*, *102*(B3), 5005–5017. doi: 10.1029/96JB03860

Zweng, M. M., Reagan, J. R., Antonov, J. I., Locarnini, R. A., Mishonov, A. V., Boyer, T. P., … Levitus, S. (2013). World ocean atlas 2013. volume 2, salinity.
doi: 10.7289/V5251G4D

Zürn, W., Beaumont, C., & Slichter, L. B. (1976). Gravity tides and ocean loading in southern alaska. *Journal of Geophysical Research (1896-1977)*, *81*(26), 4923–4932. doi: 10.1029/JB081i026p04923